# Promotional effect of Ti on mesoporous silica-supported Ru catalysts for $CO_2$ methanation

Plaifa Hongmanorom[a], Valentin Smeets[a], Aurélien Neraud[b], Ales Styskalik[c], Piyasan Praserthdam[d], Christophe Copéret[b], Damien P. Debecker[a,*]

[a] Institute of Condensed Matter and Nanosciences–Molecular, Solids and Reactivity (IMCN−MOST), Université catholique de Louvain (UCLouvain), Place Louis Pasteur, 1, box L4.01.09, 1348 Louvain-La-Neuve, Belgium

[b] Department of Chemistry and Applied Biosciences, ETH Zurich, Vladimir Prelog Weg 1−5, CH−8093 Zurich, Switzerland

[c] Department of Chemistry, Faculty of Science, Masaryk University, Kotlarska 2, Brno CZ-61137, Czech Republic

[d] Center of Excellence on Catalysis and Catalytic Reaction Engineering (CECC), Department of Chemical Engineering, Faculty of Engineering, Chulalongkorn University, Bangkok 10330, Thailand

* Corresponding Author: damien.debecker@uclouvain.be

**Abstract**

Understanding the role of metal promoter in $CO_2$ methanation is essential for advancing catalyst design and developing efficient methanation catalysts. Herein, a series of mesoporous Ti-promoted silica materials with different Ti-loadings was synthesized via the aerosol-assisted sol-gel process. These materials possess a spherical morphology with high specific surface area and homogeneous distribution of dispersed Ti species, even at Ti-loading as high as 16 mol%, thus allowing to investigate the role of Ti as a promoter in silica-supported Ru $CO_2$ methanation catalysts. Keeping the Ru loading constant, higher Ti loadings (up to 12 mol%) lead to superior catalytic activity in $CO_2$ methanation. At 300 °C, the $CH_4$ formation rate of Ru/12%Ti-$SiO_2$ catalyst (198 $\mu mol_{CH4} g_{Ru}^{-1} s^{-1}$) is 2.3 times higher than that of unpromoted Ru/$SiO_2$ catalyst (88 $\mu mol_{CH4} g_{Ru}^{-1} s^{-1}$). The improved activity correlates well with the smaller crystallite size of $RuO_2$ nanoparticles, which translates to higher Ru dispersion after reductive treatment with $H_2$. Overall, Ti helps stabilize Ru species and impedes crystal growth. With a Ti loading of 12 mol%, the crystallization of small anatase $TiO_2$ is induced after $RuO_2$ impregnation and during subsequent calcination, in turn forming the interfacial contact between Ru and $TiO_2$ after $H_2$ reduction. In-situ DRIFTS suggests that the promotion of $CO_2$ activation and CO adsorption at these interfacial sites is responsible for the enhanced catalytic activity in Ti-promoted Ru-$SiO_2$ methanation catalyst.

**Keywords:** Mesoporous silica; Titanium; Spray drying; Ruthenium; $CO_2$ methanation

## 1. Introduction

Anthropogenic carbon dioxide ($CO_2$), primarily arising from fossil fuel combustion in automobiles and industrial plants, makes up for the vast majority of greenhouse gas emissions and is the largest contributor to global warming [1, 2]. Aiming to mitigate $CO_2$ emissions into the atmosphere, it has been proposed to develop and implement $CO_2$ conversion and utilization (CCU) as an important part of $CO_2$ management strategies. Among the topmost $CO_2$ catalytic conversion processes, the hydrogenation of $CO_2$ to $CH_4$, so-called $CO_2$ methanation or Sabatier reaction, is particularly promising because of its favorable thermodynamics. Additionally, the transportation of $CH_4$ is readily feasible through existing infrastructure of natural gas pipelines [3-5]. Ultimately, it can pave the way for achieving a carbon-neutral energy balance via the process referred to as Power-to-Gas (PtG). In this process, surplus green electricity (from wind or solar energy) is utilized in $H_2O$ electrolysis to generate green $H_2$, which is then used to convert captured $CO_2$ to $CH_4$ [6, 7].

The past decade has seen rapid advances in catalyst development for $CO_2$ methanation. Both noble (e.g., Ru, Rh and Pd) and non-noble (e.g., Ni, Co and Fe) metal catalysts have been extensively studied [5, 8, 9]. Among these catalysts, Ru-based catalysts are known to be the most effective, especially at low metal loadings and low reaction temperatures [10]. Their activity and selectivity in methanation are typically governed by the nanoscale properties, such as Ru nanoparticle size and shape [11, 12], nature of the support [13-15], structural/electronic metal-support interactions [16-18] and promoter/doping effects [19, 20]. With respect to the nature of the support, a considerable amount of literature has focused on reducible oxides, including $TiO_2$ and $CeO_2$, because the presence of oxygen vacancies and the propensity of charge transfer from reducible support are thought to stabilize small Ru nanoparticles [21, 22]. Far less attention has been paid to inert oxides, $SiO_2$ in particular. Silica, a typically high specific surface area support with large pore volume, is particularly suited to disperse metal nanoparticles. $SiO_2$ also has good thermal stability, which can help steer clear of support sintering or support overgrowth on Ru sites during catalyst preparation and methanation reaction. Nevertheless, silica-supported methanation catalysts are generally shown to be only moderately active, possibly due to the absence of oxygen vacancies and basicity [13, 22]. However, strategies have emerged to improve methanation activity. For instance, ionic liquids can be employed to stabilize the dispersion of Ru nanoparticles on $SiO_2$ [23]. 1-butyl-3-methylimidazolium tetrafluoroborate ([BMIM]$BF_4$) can form a protective layer that prevents the agglomeration and oxidation of Ru nanoparticles while also providing weak and medium

basic sites. Highly dispersed small Ru nanoparticles and appropriate basic property thus result in high $CO_2$ methanation activity at low temperature. Alternatively, the presence of passivating groups (–OSi(Me)$_2$**R** with **R** = **Me** or **Bu**) at the surface of $SiO_2$ supported Ru nanoparticles was shown to promote methanation activity by lowering CO adsorption affinity on Ru nanoparticles [24]. In addition, digestion of silica from nano-Ru/nano-$SiO_2$ in the presence of Ni powder can be employed to disassemble large Ru agglomerates on $SiO_2$ into smaller Ru nanoparticles on the Ni surface with an oxide passivation layer. The synthesized oxide passivated Ni-supported Ru nanoparticles, in which unalloyed bimetallic nano-Ru and Ni are formed, are highly active and stable in low-temperature $CO_2$ methanation [25].

The aerosol-assisted sol-gel process has been proposed as a versatile and highly potent method for preparing nanostructured materials with high specific surface area, well-defined pore size and tuneable texture and composition. This process integrates sol-gel chemistry, aerosol spray drying and evaporation-induced self-assembly in one step and in a continuous mode of rapid nanomaterials production [26, 27]. It offers a possibility to incorporate a variety of metals (oxides), such as Ti , Ga , Zn, Ta, W and alloyed PdNi, into silica supports [26, 28]. These materials can also accommodate high loading of the promoter while maintaining homogeneous dispersion.

In the present study, we have leveraged the aerosol-assisted sol-gel process to prepare hierarchical mesoporous Ti-promoted silica supports for Ru-based methanation catalysts. Ti is chosen as the promoter considering that the combination between Ru and Ti is one of the most promising catalyst formulations for $CO_2$ methanation [5, 8]. In addition, this method enables us to unravel the effects of Ti promoter on the catalytic performance of silica supported Ru catalysts in $CO_2$ methanation.

## 2. Experimental

### 2.1. Preparation of mesoporous Ti-$SiO_2$ support materials

A series of mesoporous Ti-$SiO_2$ support materials was synthesized via the aerosol-assisted sol-gel process following similar procedure reported by Smeets et al. [29] and varying Ti loading. First, titanium butoxide (TiBuO, Fluka, 99%) was added dropwise into aqueous tetrapropylammonium hydroxide (TPAOH, Merck, 40% w/w) and stirred for 10 min, followed by addition of distilled water. After stirring for another 10 min, tetraethyl orthosilicate (TEOS, Sigma, 98%) was added into the solution and thoroughly mixed overnight to hydrolyze the precursors. The precursor solution was subsequently aged at 70 °C for 15 h. Pluronic F127

surfactant was then added and vigorously stirred at room temperature until complete dissolution. The molar ratio of the components was 1 $SiO_2$: X $TiO_2$: Y TPAOH: 0.005 F127: 17 $H_2O$ with different Ti loadings (mol Ti / (mol Ti + mol Si) x 100% = 0, 4, 8, 12 and 16%) and a constant TPAOH to (Si + Ti) ratio of 0.15. The exact masses of reagents are summarized in Table S1. The clear yellowish solution was sprayed by a Büchi Mini Spray Dryer B-290 under 4-bar air pressure, and the aerosol was carried by air to pass through a drying chamber heated at 150 °C. The dried powder was further aged at 70 °C overnight before calcination in air at 550 °C for 5 h with a heating rate of 5 °C/min. The obtained supports are denoted as x%Ti-$SiO_2$, where x means mol% Ti loading.

### 2.2. Preparation of Ru/Ti-$SiO_2$ catalysts

The Ru-based catalysts (2 wt% Ru nominal loading) were prepared by wet impregnation of aerosol supports with $RuO_2$ nanoparticles. The $RuO_2$ colloidal suspension was pre-synthesized as described elsewhere [30]. First, 0.81 mmol of $RuCl_3$ was dissolved in 40 mL of distilled water under stirring. Next, 23 mL of aqueous hydrogen peroxide (14%) was added dropwise and mixed for 5 min. The solution was then incubated in an oven at 95 °C for 2 h to obtain a black $RuO_2$ colloidal suspension. After cooling to room temperature, 4 g of aerosol-made support was added into the entire batch of $RuO_2$ colloidal suspension and stirred while heating at 50 °C for 16 h. The solution was evaporated by a rotavapor set at 50 °C under vacuum, and the obtained powder was finally calcined in static air at 450 °C for 16 h with a ramping rate of 5 °C/min. These catalysts are denoted as Ru/x%Ti-$SiO_2$ (x is mol% of Ti loading).

### 2.3. Characterization

Fourier transform infrared (FTIR) spectra were recorded using a Bruker EQUINOX 55 spectrometer. The mixture of sample and KBr (0.5 wt% sample in KBr) was finely ground and pelletized. 100 scans were measured between 400 and 4000 $cm^{-1}$ with a spectral resolution of 2 $cm^{-1}$.

Diffuse reflectance UV-visible (DRUV-vis) spectra were collected by a Shimadzu UV-3600 Plus spectrophotometer. Spectralon pellet was used as a reference material to correct the background. The sample powder was then loaded into the holder and scanned in the range of 200-400 nm. The obtained data were displayed in Kubelka Munk function.

X-ray photoelectron spectroscopy (XPS) experiment was carried out by an SSX 100/206 spectrometer from Surface Science Instruments, USA equipped with Al-Kα radiation operated

at 10 kV and 20 mA. The binding energy was calibrated by the position of Si 2p peak fixed at 103.5 eV, and data treatment and processing were done with CasaXPS software.

The weight percentages of Ti and Ru were measured by inductively coupled plasma atomic emission spectroscopy (ICP-AES) on an iCAP 6500 instrument (Thermo Scientific Instrument). Prior to the measurement, the sample was dissolved by sodium peroxide fusion.

Textural properties of supports and fresh catalysts were evaluated from $N_2$ physisorption isotherms at -196 °C using a Tristar 3000 instrument (Micromeritics). The sample was degassed under vacuum at 170 °C overnight before the measurement so as to remove physisorbed water and other volatile contaminants. The specific surface area was determined by the Brunauer-Emmett-Teller (BET) method applied in a low range of relative pressure ($P/P_0$) from 0.01 to 0.1, taking the presence of micropores into account [29]. The total pore volume was estimated from the adsorption branch at $P/P_0 \sim 0.98$, while the pore size distribution was obtained from the adsorption branch using the Barrett-Joyner-Halenda (BJH) method.

Transmission electron microscopy (TEM) measurement was performed using a JEOL-JEM 2100 system equipped with an EDX detector. To prepare a TEM sample, the sample powder was put into ethanol and sonicated to obtain the suspension, which was subsequently dropped onto the copper grid. STEM-EDS measurements were carried out on a Thermo Fisher Scientific Talos F200C instrument equipped with Bruker Xflash 6T-30 EDS detector, High angle angular dark field detector (HAADF) for STEM imaging and a Thermo Fisher Scientific Ceta 16-megapixel CMOS camera. Powders were dispersed in cyclohexane, and 4 μL was deposited on a gold grid covered by QuantiFoil® holey carbon, filtered and then dried in air.

X-ray diffraction (XRD) measurement was performed using a Bruker AXS-D8 Advance diffractometer using Cu Kα ($\lambda$ = 0.15418 nm) radiation at 30 kV and 40 mA. The 2θ diffractograms were recorded between 10 and 60° with a step size of 0.025° and a step time of 20 $s \cdot step^{-1}$.

$H_2$-temperature programmed reduction ($H_2$-TPR) and $CO_2$-temperature programmed reduction ($CO_2$-TPD) experiments were conducted on a Hiden instrument equipped with an online QGA mass spectrometer (MS). In $H_2$-TPR measurement, about 30 mg of catalyst was first outgassed under Ar flow of 20 mL/min at 100 °C to eliminate physisorbed water and impurities. After that, the MS signals were recorded as a function of temperature from 100 °C to 450 °C with a heating rate of 10 °C/min under 40 mL/min of 2.5% (v/v) $H_2$ diluted in inert gases

[2.5:82.5:15% (v/v) $H_2$/He/Ar]. In $CO_2$-TPD measurement, about 50 mg of catalyst was in-situ reduced at 200 °C under 20 mL/min of 5%$H_2$/Ar for 1 h, followed by purging under 20 mL/min of Ar for 1 h and then cooling down to 50 °C. At this temperature, $CO_2$ adsorption (15% $CO_2$/Ar) was done for 1 h. Physically adsorbed $CO_2$ was subsequently removed under 20 mL/min of Ar for 1 h. Finally, the MS signals were recorded as a function of temperature from 50 °C to 800 °C (10 °C/min) under 20 mL/min of Ar.

$H_2$ pulse chemisorption measurement was carried out on a BELCAT II analyzer (Microtrac). Before the pulse chemisorption, about 150 mg of catalyst was reduced at 200 °C for 2 h under 30 mL/min of 5% $H_2$/Ar and purged for 1 h under 30 mL/min of Ar. After cooling down to 100 °C, the $H_2$ pulses were injected with a loop volume of 0.989 mL. The chemisorption stoichiometry of H/Ru = 1 was used for calculating the Ru dispersion [13].

In-situ $CO_2$ methanation diffuse reflectance infrared Fourier transform spectroscopy (DRIFTS) experiment was carried out using a Bruker INVENIO-S spectrometer. The catalyst was in-situ reduced in a Harrick Praying Mantis chamber at 200 °C under $H_2$ for 1 h and flushed under He for 30 min. A background spectrum was then taken in He atmosphere for each reaction temperature. For background subtraction, the spectra were scaled such that the $\nu_{Si-O}$ vibrational frequency at 1865 $cm^{-1}$ was absent [24, 31]. During $CO_2$ methanation DRIFTS experiment, a gas mixture comprising 8 mol% $CO_2$, 32 mol% $H_2$ and He balance was flowed into the chamber, which was set to the desired temperature from 50 °C to 300 °C. The spectra were collected after a steady state was attained at each temperature.

### 2.4. Catalytic activity evaluation

The $CO_2$ methanation performance was evaluated in a continuous flow fixed-bed reactor. A total of 100 mg of catalyst (pressed and sieved in the 100-315 μm range) was in-situ reduced in the reactor at 200 °C for 1 h under 30 mL/min of $H_2$ and purged at the same temperature for 1 h under 10 mL/min of Ar. A reaction mixture of 10% $CO_2$ and 40% $H_2$ diluted in Ar (total flow rate of 20 mL/min) was then introduced into the reactor. The reaction was performed at atmospheric pressure in the step mode from 200 °C to 300 °C with 25 °C intervals, and at least four gas chromatography injections were done for each temperature after reaching a steady state. The outlet gases were quantified by a gas chromatograph (SCION 456-GC) equipped with Hayesep Q, Molsieve 5A, Porapak R and SCION-1 columns. The separated CO and $CO_2$ were analyzed by a thermal conductivity detector, while $CH_4$ was detected with a flame ionization detector. During the reaction, all gas transfer lines were maintained at 110 °C so that

the condensation of water by-product was prevented. $CO_2$ conversion ($X_{CO_2}$), $CH_4$ selectivity ($S_{CH_4}$), and $CH_4$ formation rate ($r_{CH_4}$) were calculated according to the following equations:

$$X_{CO_2}(\%) = \frac{F_{CO_{2,in}} - F_{CO_{2,out}}}{F_{CO_{2,in}}} \times 100\% \quad (1)$$

$$S_{CH_4}(\%) = \frac{F_{CH_{4,out}}}{F_{CO_{2,in}} - F_{CO_{2,out}}} \times 100\% \quad (2)$$

$$r_{CH_4}(\mu mol_{CH_4} g_{Ru}^{-1} s^{-1}) = \frac{F_{CH_{4,out}}}{m_{Ru}} \quad (3)$$

where F is the molar flow rate, and $m_{Ru}$ is the mass of Ru measured by ICP-AES.

## 3. Results and discussion

### 3.1. Preparation and characterization of mesoporous x%Ti-$SiO_2$ supports and Ru/x%Ti-$SiO_2$ catalysts

#### 3.1.1. Mesoporous x%Ti-$SiO_2$ supports

**Table 1** Textural properties of $SiO_2$ and Ti-$SiO_2$ supports and freshly calcined Ru/$SiO_2$ and Ru/Ti-$SiO_2$ catalysts.

| Support | BET surface area ($m^2/g$) [a] | Pore volume ($cm^3/g$) [b] | Catalyst | BET surface area ($m^2/g$) [a] | Pore volume ($cm^3/g$) [b] |
|---|---|---|---|---|---|
| $SiO_2$ | 631 | 0.74 (0.07) | Ru/$SiO_2$ | 527 | 0.63 (0.04) |
| 4%Ti-$SiO_2$ | 616 | 0.69 (0.08) | Ru/4%Ti-$SiO_2$ | 543 | 0.65 (0.06) |
| 8%Ti-$SiO_2$ | 618 | 0.71 (0.08) | Ru/8%Ti-$SiO_2$ | 550 | 0.66 (0.06) |
| 12%Ti-$SiO_2$ | 528 | 0.62 (0.06) | Ru/12%Ti-$SiO_2$ | 456 | 0.54 (0.06) |
| 16%Ti-$SiO_2$ | 491 | 0.60 (0.06) | Ru/16%Ti-$SiO_2$ | 421 | 0.49 (0.06) |

[a] The Brunauer-Emmett-Teller (BET) method was applied in a low range of relative pressure ($P/P_0$) from 0.01 to 0.1, taking the presence of micropores into account. [b] The total pore volume was measured at $P/P_0 \sim 0.98$. The micropore volume estimated from the t-plot is shown in parentheses.

The mesoporous x%Ti-$SiO_2$ supports were prepared by the aerosol-assisted sol-gel process [29], with different Ti loadings (x = 0, 4, 8, 12 and 16%). $N_2$ physisorption isotherms and BJH pore size distributions are displayed in Fig. 1 (a) and (b), and their textural properties are summarized in Table 1. All isotherms correspond to Type IV isotherms, consistent with mesoporous solids. Pore size distributions of all aerosol silica are centered in the same range *ca.* 12-15 nm. This pore size is larger than the expected size of F127 micelles (*ca.* 5-6 nm) due

to the swelling effect from the incorporation of $TPA^+$ cations during the synthesis [29]. Notably, the BET surface area ($S_{BET}$) and total pore volume ($V_p$) decrease with increasing Ti loadings across the sample series.

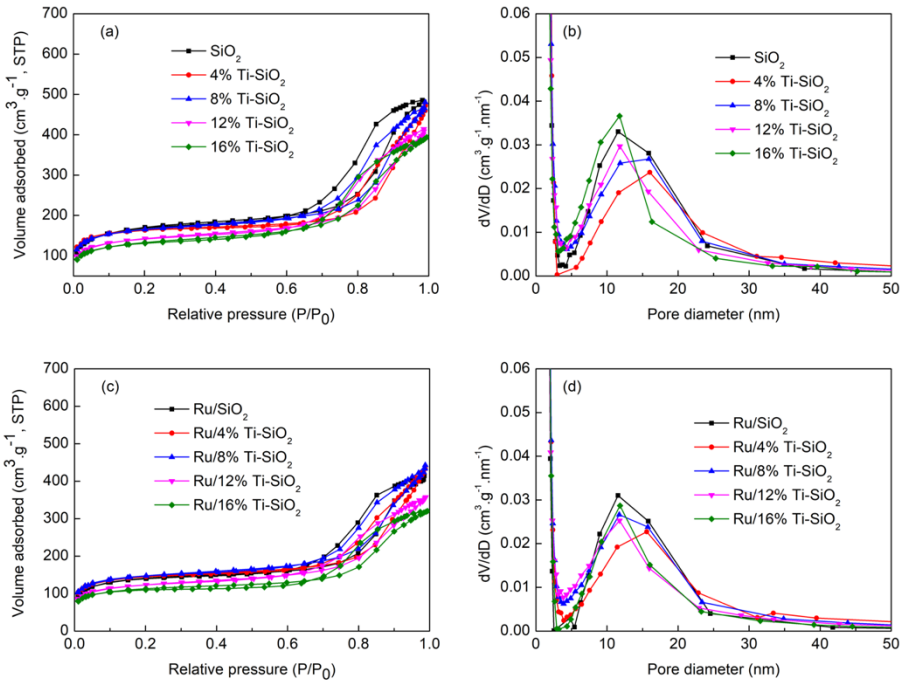


**Fig. 1** $N_2$ physisorption analyses of (a) and (b) $SiO_2$ and Ti-$SiO_2$ supports and (c) and (d) freshly calcined Ru/$SiO_2$ and Ru/Ti-$SiO_2$ catalysts. (a) and (c) are $N_2$ physisorption isotherms. (b) and (d) are BJH pore-size distributions.

The high dispersion of Ti across the supports was confirmed by DRUV-vis (Fig. 2) and XRD analyses. In Fig. 2(a), the band centered at *ca.* 215-245 nm is associated with ligand-to-metal charge transfer (LMCT) bands, that correspond to isolated tetrahedral $TiO_4$ coordination, while the band in the 250-300 nm range can be attributed to the presence of Ti in higher coordination, such as water-coordinated Ti species, oligomeric Ti species or polymerized $TiO_4$ and $TiO_5$ species [32, 33]. With an increase of Ti loading from 4% to 16%, the maximum absorption band shifts from 215 nm to 255 nm, suggesting larger amounts of Ti in higher coordination number than tetrahedral due to higher Ti polymerization. However, the characteristic band of octahedral $TiO_6$ as in bulk $TiO_2$ nanocrystals (i.e., anatase) at around 330 nm is never observed [34]. Analysis of the band gap ($E_g$) also demonstrates that Ti atoms are mostly highly dispersed in the $SiO_2$ matrix, even if a growing but minor fraction is present in the forms of oligomeric or small nanodomains of $TiO_x$ species when the Ti loading increases (see Supporting Information, Fig. S1). Consistent with the DR UV-vis results, the XRD patterns of all Ti-$SiO_2$

materials (Fig. S2) solely exhibit amorphous features without any $TiO_2$ crystalline phase, albeit high Ti loading up to 16% [29].

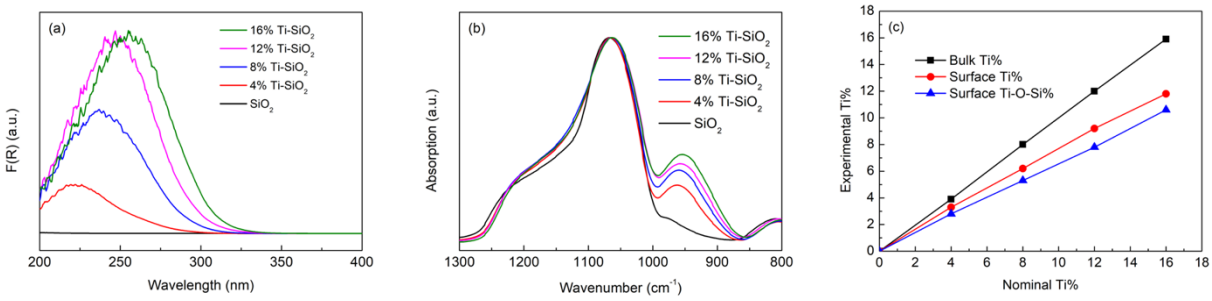


**Fig. 2** (a) DRUV-visible spectra (Kubelka-Munk Function), (b) FTIR-ATR spectra and (c) Experimental Ti% measured by ICP-AES and XPS against nominal Ti% as shown in Table 2 of Ti-$SiO_2$ supports.

In Fig. 2(b), FTIR spectroscopy provides information on the formation of Si–O–Ti bonds at ~960 $cm^{-1}$ band [35, 36]. This band becomes stronger with increased Ti loadings, indicating more substitution of $Si^{4+}$ ions by tetrahedral $Ti^{4+}$ ions in the matrix of Ti-$SiO_2$ materials. The pristine $SiO_2$ (without Ti) exhibits only the main bands at ~1080 and 800 $cm^{-1}$ ascribed to the asymmetric and symmetric Si–O–Si vibration, respectively, and a weak band at ~975 $cm^{-1}$ related to the symmetric stretching of silanol Si–O–H groups [37].

**Table 2** The band gap energy ($E_g$) and bulk and surface composition of Ti species in Ti-$SiO_2$ supports.

| Support | $E_g$ (eV) [a] | Nominal Ti (%) | ICP-AES Bulk Ti (%) | XPS | |
|---|---|---|---|---|---|
| | | | | Total Surface Ti (%) | Surface Ti-O-Si (%) |
| 4%Ti-$SiO_2$ | 4.88 | 4 | 3.9 | 3.3 | 2.8 |
| 8%Ti-$SiO_2$ | 4.50 | 8 | 8 | 6.2 | 5.3 |
| 12%Ti-$SiO_2$ | 4.41 | 12 | 12 | 9.2 | 7.8 |
| 16%Ti-$SiO_2$ | 4.28 | 16 | 15.9 | 11.8 | 10.6 |

[a] The band gap energy was obtained from the optical absorption edges in the DR UV-visible spectra of Ti-$SiO_2$ supports (Fig. S1).

The surface composition and dispersion of Ti species were further determined by XPS. Two fractions of Ti species detected at the surface can be distinguished from Ti $2p_{3/2}$ peak deconvolution (Fig. S3). Considering that the binding energy (BE) values of *ca.* 460.0 eV and

458.5 eV are assigned to the fractions of Ti incorporated in the $SiO_2$ matrix (Ti–O–Si) and Ti present as the nanodomains (Ti–O–Ti), respectively [29, 38], the percentages of total Ti and silica-incorporated Ti species at the surface can be quantified (Table 2). Notably, the measured surface Ti % and Ti–O–Si % contents (XPS) vs. the nominal Ti loadings show a linear relationship up to 16% Ti loading (Fig. 2(c)). Similarly, a linear relationship with a slope of 1 can be found between the bulk Ti% measured from ICP-AES and the nominal Ti%, demonstrating an excellent quantitative control of the bulk composition in Ti-$SiO_2$ materials prepared by aerosol method. Besides, the surface Ti concentration is close to the bulk content, showing homogeneous spatial distribution of Ti species in bulk and surface.

### 3.1.2 Ru/x%-$SiO_2$ catalysts

The silica-supported Ru catalysts were prepared by wetness impregnation of silica supports with a stable monodispersed $RuO_2$ colloidal suspension (~2 nm), pre-synthesized from the reaction between $RuCl_3$ and $H_2O_2$ according to a reported method [30].The introduction of $RuO_2$ followed by calcination slightly reduces $S_{BET}$ and $V_p$ (Table 1), while the shape of the Type IV isotherms (Fig. 1(c)) and the pore size distributions (Fig. 1(d)) remain essentially the same for all catalysts. These results suggest that there is no significant modification of the mesoscopic order after the impregnation of Ru species into aerosol silica.

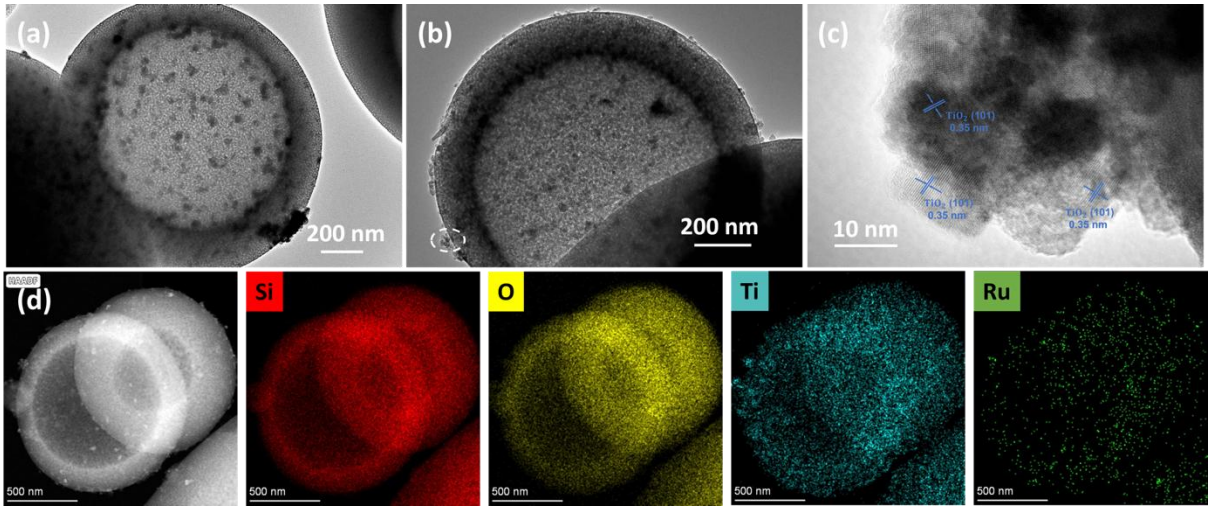


**Fig. 3** TEM images of freshly calcined (a) Ru/$SiO_2$ and (b) Ru/12%Ti-$SiO_2$. (c) High magnification TEM image of white dashed ellipse in (b), showing the (101) crystal planes of anatase $TiO_2$. (d) HAADF-STEM-EDS mapping images of reduced Ru/12%Ti-$SiO_2$ catalyst.

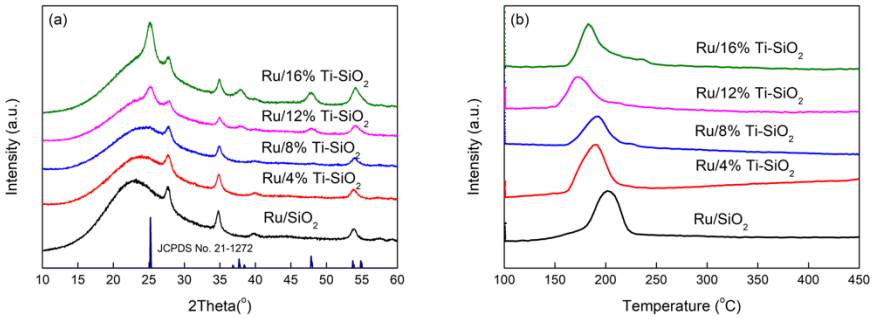


**Fig. 4** (a) XRD patterns and (b) $H_2$-TPR profiles of freshly calcined $Ru/SiO_2$ and $Ru/Ti\text{-}SiO_2$ catalysts.

TEM images (Fig. 3 and Fig. S4) illustrate the morphology and structure of Ru-based catalysts as well as how $Ru/RuO_2$ nanoparticles are dispersed over aerosol materials. All $Ru/x\%Ti\text{-}SiO_2$ catalysts possess a spherical morphology with microsphere sizes ranging between 0.2 and 1 μm, as the spherical shape is the most stable form during the drying of liquid droplets. Hollow structure can be formed when drying happens rapidly at the droplet surface, quickly creating a solid layer [26]. A regular porous structure with mesopores is also visible, which is consistent with the $N_2$ physisorption results. In Fig. 3(a), large $RuO_2$ crystallites are clearly visible when no Ti is present. $RuO_2$ nanoparticles are mainly located inside the spheres, stemming from the introduction of $RuO_2$ aqueous suspension through the mesoporous network during impregnation. $RuO_2$ aggregates can also be noticed on the surface. These large $RuO_2$ crystallites correspondingly appear in the XRD pattern (Fig. 4(a)) as sharp diffraction peaks at $2\theta = 27.9$ (110), 34.9 (101), 39.9 (200) and 54.0° (211) (JCPDS No. 43-1027). Compared with $Ru/SiO_2$, $Ru/12\%Ti\text{-}SiO_2$ visually features much smaller $RuO_2$ nanoparticles (Fig. 3(b)), while HAADF-STEM-EDS mapping in Fig. 3(d) displays homogeneous distribution of Ti and Ru species over reduced $Ru/12\%Ti\text{-}SiO_2$ catalyst. Interestingly, crystal lattices corresponding to the (101) plane of anatase $TiO_2$ (0.35 nm) are apparent in high magnification TEM image (Fig. 3(c)), which agrees well with the XRD result. The crystalline phase of anatase $TiO_2$ (JCPDS No. 21-1272) becomes distinct in the XRD pattern of $Ru/12\%Ti\text{-}SiO_2$ catalyst in Fig. 4(a) upon calcination at 450 °C (lower than the calcination temperature applied for bare $x\%Ti\text{-}SiO_2$ supports, 550 °C) after $RuO_2$ impregnation. These findings suggest that $RuO_2$ nanoparticles promote the crystallization of amorphous $TiO_2$, and point to the generation of $RuO_2\text{-}TiO_2$ interface. The anatase $TiO_2$ phase has an average crystallite size of 7.2 nm in both $Ru/12\%Ti\text{-}SiO_2$ and $Ru/16\%Ti\text{-}SiO_2$ catalysts, as determined by the Scherrer equation from the width of the (101) peak at 25.4°. Although $TiO_2$ crystalline phases are only visible in the XRD patterns

of Ru/12%Ti-$SiO_2$ and Ru/16%Ti-$SiO_2$ catalysts, the $TiO_2$ crystallization induced by wetness impregnation with $RuO_2$ colloidal suspension occurs for all catalysts, as indicated by a decrease in their $E_g$ values (Fig. S5 and Table S2). The HAADF-STEM-EDS mapping images of reduced Ru/$SiO_2$, Ru/4%Ti-$SiO_2$, Ru/8%Ti-$SiO_2$ and Ru/16%Ti-$SiO_2$ catalysts are also shown in Fig. S4. It is evident that Ru nanoparticles in Ti-promoted catalysts are less agglomerated as compared to those in Ru/$SiO_2$. It is noted that Ru/$RuO_2$ particle sizes cannot be univocally estimated from TEM images owing to their aggregation in the case of Ru/$SiO_2$ catalyst and unclear distinction between Ru and Ti species in the case of Ti-containing catalysts.

**Table 3** $RuO_2$ crystallite size, Ru dispersion, surface and bulk composition of Ti and Ru species in freshly calcined and spent catalysts.

| Catalyst | $RuO_2$ crystallite size (nm) [a] | Ru dispersion (%) [b] | XPS (Freshly calcined) | | XPS (Spent) | | ICP-AES Ru (wt%) |
|---|---|---|---|---|---|---|---|
| | | | Total surface Ti (%) | Ru/(Si+Ti) | Total surface Ti (%) | Ru/(Si+Ti) | |
| Ru/$SiO_2$ | 13.5 | 0.1±0.04 | 0 | 0.030 | 0 | 0.028 | 1.5 |
| Ru/4%Ti-$SiO_2$ | 12.1 | 2.5 | 2.5 | 0.026 | 2.9 | 0.029 | 1.9 |
| Ru/8%Ti-$SiO_2$ | 11.4 | 3.7 | 6.6 | 0.027 | 7.6 | 0.028 | 1.7 |
| Ru/12%Ti-$SiO_2$ | 9.1 | 7.4 | 11.5 | 0.015 | 11.2 | 0.018 | 1.8 |
| Ru/16%Ti-$SiO_2$ | 12.0 | 5.3 | 14.3 | 0.024 | 15.1 | 0.025 | 1.8 |

[a] $RuO_2$ crystallite size was obtained from the average between (110) and (101) planes of $RuO_2$ in the XRD patterns using Scherrer equation.

[b] Ru dispersion was determined from $H_2$ pulse chemisorption measurement.

For comparison, the crystallite sizes of $RuO_2$ are calculated via the Scherrer equation. As listed in Table 3, the higher the Ti loading up to 12%, the smaller the $RuO_2$ crystallite size in calcined catalysts. $H_2$ pulse chemisorption was also performed to quantitatively estimate the dispersion of Ru (Table 3). The Ru dispersion on Ru/$SiO_2$ is extremely poor, 0.1±0.04% (acknowledging the non-uniform distribution and agglomeration of Ru nanoparticles), but the Ru dispersion increases with the increase in Ti-content, reaching the highest at 12 mol% (2.5%, 3.7%, 7.4% and 5.3% for Ru/4%Ti-$SiO_2$, Ru/8%Ti-$SiO_2$, Ru/12%Ti-$SiO_2$ and Ru/16%Ti-$SiO_2$, respectively). All in all, the presence of Ti has a beneficial role in stabilizing Ru/$RuO_2$ nanoparticles, thus impeding their growth and aggregation during the calcination and reduction. One may notice discrepancies between the sizes of Ru nanoparticles estimated from

XRD and $H_2$ pulse chemisorption. From XRD analysis, assuming that $RuO_2$ particles shrink by around 24% during the reduction due to the difference in mass density between $RuO_2$ and Ru [39], Ru crystallite sizes are expected to be 9.2 nm, 8.7 nm, 6.9 nm and 9.1 nm for Ru/4%Ti-$SiO_2$, Ru/8%Ti-$SiO_2$, Ru/12%Ti-$SiO_2$ and Ru/16%Ti-$SiO_2$, respectively. From $H_2$ pulse chemisorption (details on the calculation found elsewhere [13]), Ru particle sizes are 37.3 nm, 25.4 nm, 12.8 nm and 17.9 nm for the same samples. The differences may arise, as XRD measures diffracting crystallites planes rather than entire particles [40]. Additionally, weak or slow kinetics of $H_2$ chemisorption may lead to underestimation of Ru dispersion measured by $H_2$ pulse chemisorption, as reported in previous studies [41, 42].

The reducibility of Ru/x%Ti-$SiO_2$ catalysts was investigated using $H_2$-TPR. The shape of $H_2$-TPR profile is similar among all catalysts in Fig. 4(b). One main peak can be observed and ascribed to the reduction of oxidic Ru species. This reduction peak is centered at around 200 °C for Ru/$SiO_2$ and shifted toward lower temperatures with higher Ti loading up to 12%, followed by a shift toward higher temperature for 16% Ti loading. Enhanced reducibility with increased Ti loading is possibly related to the stabilization of smaller $RuO_2$ nanoparticles by Ti species. Notably, it has been reported that smaller $RuO_2$ nanoparticles have lower activation energy for hydrogen dissociation [43].

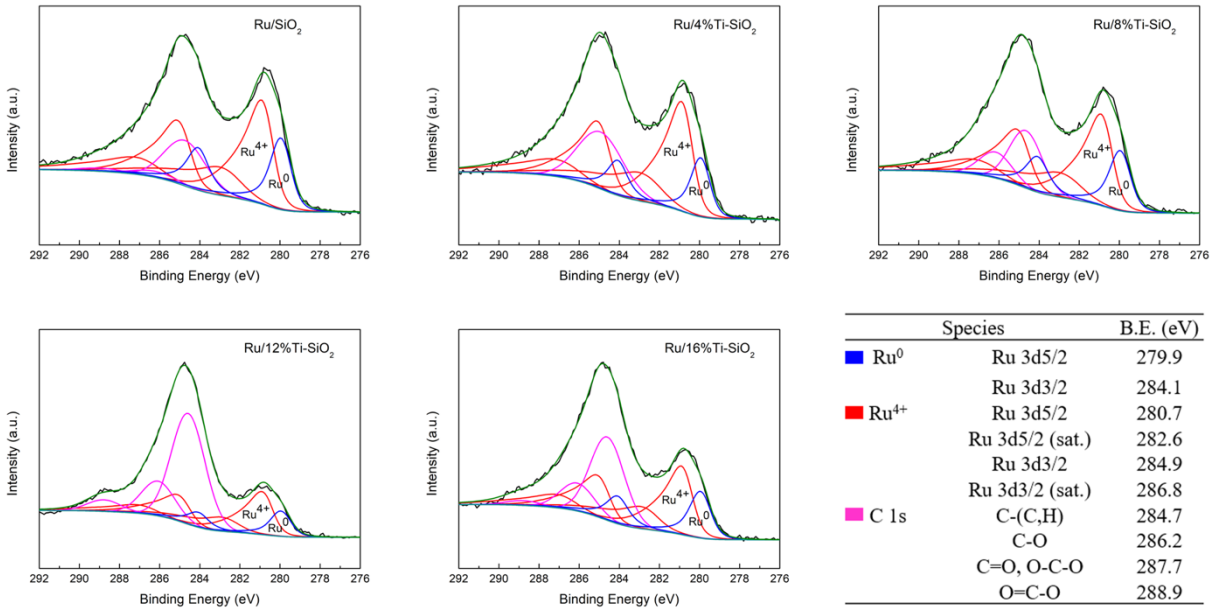


| | Species | B.E. (eV) |
|---|---|---|
| $Ru^0$ | Ru 3d5/2 | 279.9 |
| | Ru 3d3/2 | 284.1 |
| $Ru^{4+}$ | Ru 3d5/2 | 280.7 |
| | Ru 3d5/2 (sat.) | 282.6 |
| | Ru 3d3/2 | 284.9 |
| | Ru 3d3/2 (sat.) | 286.8 |
| C 1s | C-(C,H) | 284.7 |
| | C-O | 286.2 |
| | C=O, O-C-O | 287.7 |
| | O=C-O | 288.9 |

**Fig. 5** XPS spectra of C 1s and Ru 3d regions of freshly calcined Ru/$SiO_2$ and Ru/Ti-$SiO_2$ catalysts.

The chemical state and surface compositions after $RuO_2$ deposition and calcination were also determined by XPS (Fig. 5 and Fig. S6). Table 3 shows the percentage of Ti species at the

Ru/x%Ti-$SiO_2$ surface, which can be compared to that at the x%Ti-$SiO_2$ surface in Table 2. Slightly higher surface Ti concentration of Ru/12%Ti-$SiO_2$ and Ru/16%Ti-$SiO_2$ corroborates the finding that $TiO_2$ crystals form on the catalyst surface. Fig. 5 presents the spectra of Ru 3d and C 1s of freshly calcined Ru/x%Ti-$SiO_2$ catalysts. The spectra can be deconvoluted into three components, including metallic Ru, oxidized $Ru^{4+}$ and C 1s components, as tabulated in Fig. 5. A doublet with an asymmetric shape at 279.9 eV belongs to metallic Ru, whereas a main doublet at 280.7 eV along with a satellite doublet at 282.6 eV represents oxidized $Ru^{4+}$ state. These signals are fitted using two symmetric Gaussian−Lorentzian functions with separated binding energy (B.E.) of 4.17 eV and area ratio of 3:2. The satellite and the main doublet are separated by about 1.9 eV with close to 50% ratio. It is noted that C 1s components overlap with Ru 3d3/2 components; thus, the signals are fitted using Gaussian−Lorentzian functions, in which full width at half-maximum (fwhm) and binding-energy constraints are kept consistent across all spectra [44]. The surface Ru/(Si+Ti) atomic ratio obtained from XPS analysis and Ru content measured from ICP-AES are shown in Table 3. Ru/$SiO_2$ has a surface Ru/(Si+Ti) ratio of 0.03, while other Ti-containing catalysts, especially Ru/12%Ti-$SiO_2$, exhibit lower surface Ru/(Si+Ti) ratio. This finding indicates that Ru species are highly dispersed in the pores rather than being aggregated on the surface of Ti-containing catalyst microspheres.

### 3.2. Catalytic performance

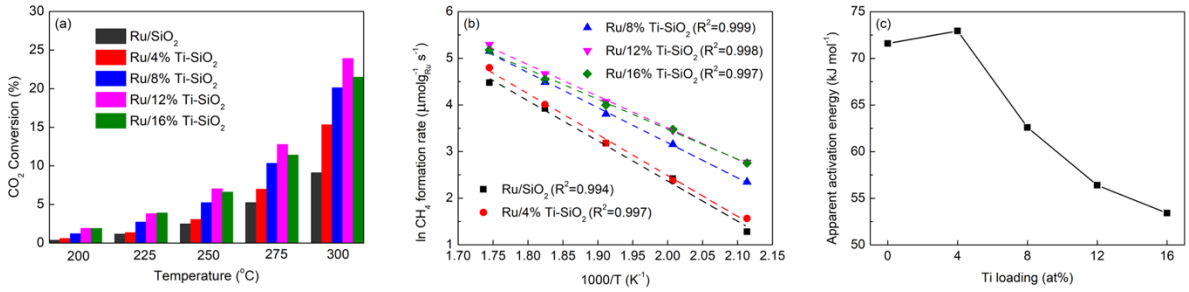


**Fig. 6** (a) $CO_2$ conversion as a function of temperature from 200 °C to 300 °C, (b) Arrhenius plot of $CH_4$ formation rate over Ru/$SiO_2$ and Ru/Ti-$SiO_2$ catalysts in the temperature range of 200-300 °C and (c) Apparent activation energy (from Fig. 6(b)) as a function of Ti loading.

Catalytic $CO_2$ methanation was performed in the temperature range between 200 and 300 °C. The reaction conditions were chosen such that $CO_2$ conversion remained far below the thermodynamic limit at all temperatures, ensuring the measurement of intrinsic activity (kinetic regime; see Fig. S7 in the Supporting Information). In Fig. 6(a), $CO_2$ conversion obtained with

catalysts with different Ti loadings follows the trend of $Ru/SiO_2$ < $Ru/4\%Ti\text{-}SiO_2$ < $Ru/8\%Ti\text{-}SiO_2$ < $Ru/16\%Ti\text{-}SiO_2$ < $Ru/12\%Ti\text{-}SiO_2$. All $Ru/x\%Ti\text{-}SiO_2$ catalysts exhibit 100% selectivity toward $CH_4$ over the whole temperature range, whereas the level of activity is shown to be greatly affected by the Ti loading. The corresponding $CH_4$ formation rate at 300 °C normalized by the Ru mass measured from ICP-AES is provided in Table S3. It should be acknowledged that these rates are lower than the rates typically reported for benchmark $Ru/TiO_2$ [15]. Yet, focusing on the doping effect of Ti in the $Ru/SiO_2$ system, it is striking to observe that the $CH_4$ formation rate of $Ru/12\%Ti\text{-}SiO_2$ is 2.3 times higher than that of the non-promoted $Ru/SiO_2$. Furthermore, a good correlation can be found between Ru dispersion and catalytic performance in $CO_2$ methanation, i.e., the higher the Ru dispersion, the superior the $CH_4$ formation rate.

In an attempt to better understand the decisive role of Ti promoter, the apparent activation energies ($E_a$) for $CO_2$ methanation are also calculated. They are based on the reaction rates in the temperature range from 200 °C to 300 °C as presented in the Arrhenius plot (Fig. 6(b)) and then plotted as a function of Ti loading in Fig. 6(c). The obtained $E_a$ values are between 53 and 73 kJ/mol, falling within the range typically reported for Ru-based catalysts [15, 20, 45]. The apparent activation energies for the catalysts with 0% and 4% are about the same but decrease significantly as the Ti loading increases to 8% and 12%, then the value remains similar for 16%. The drop in the apparent activation energy suggests that the nature of the active sites is modified. This modification could affect the CO adsorption energy or even the reaction mechanism (vide infra in the section 3.4.). A change in the reaction mechanism is however rather unlikely, considering a single linear compensation line in the Constable plot in Fig. S8 (In (A) vs. $E_a$, where A represents the preexponential factor in the Arrhenius equation derived from plots in Fig. 6(b)) [46].

Both $Ru/SiO_2$ and $Ru/12\%Ti\text{-}SiO_2$ underwent further testing at 300 °C for 50 h to assess their stability. As shown in Fig. S9, their selectivity to $CH_4$ remains at 100% throughout 50 h runtime. Surprisingly, $Ru/12\%Ti\text{-}SiO_2$ exhibits a gradual increase in $CO_2$ conversion from 24% to 39% within the first 10 h and stabilizes thereafter. The observation of induction period suggests that more active sites may be formed during the introduction of $CO_2/H_2$ at 300 °C (higher than the reduction temperature of 200 °C). This could be due to a more pronounced interface formation between Ru and $TiO_2$ under the reaction gas mixtures at high temperature [17]. In contrast, $Ru/SiO_2$ exhibits continuous activity loss from 8% to 4% during 50 h on stream, likely due to the sintering of Ru nanoparticles.

### 3.3. Characterization of spent Ru/Ti-$SiO_2$ catalysts

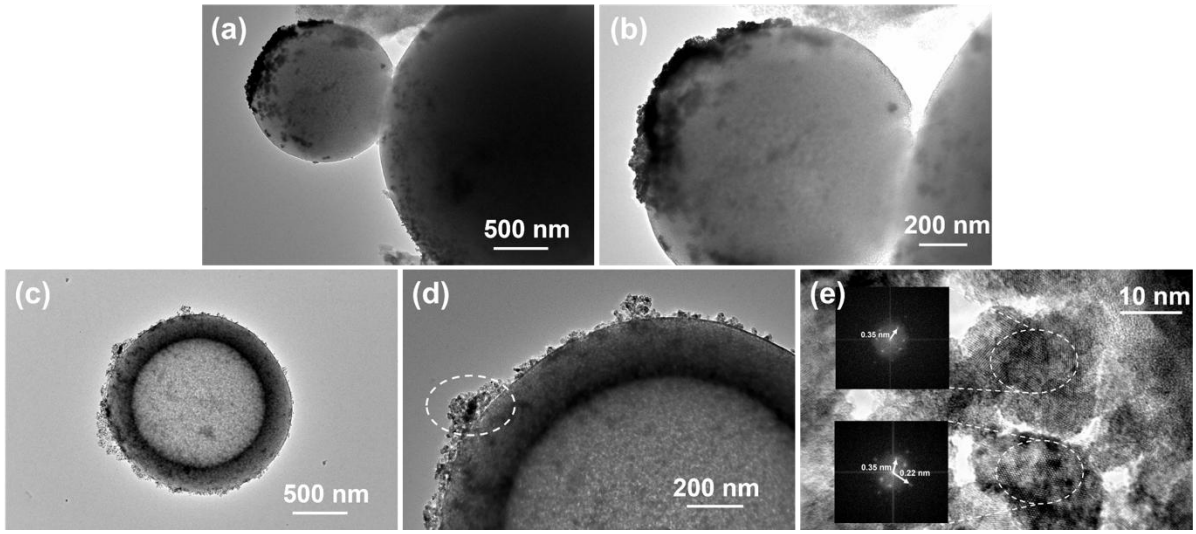


**Fig. 7** TEM images of spent Ru/$SiO_2$ (a and b) and Ru/12%Ti-$SiO_2$ (c and d). (e) High magnification TEM image of white dashed ellipse in (d), showing the (101) crystal planes of anatase $TiO_2$ and Ru determined from Fast Fourier Transform (FFT) patterns in the insets.

After the methanation reaction, spent Ru/x%Ti-$SiO_2$ catalysts were subjected to TEM, XRD and XPS analyses. TEM images of spent catalysts in Fig. 7 illustrate that the sphere-like morphology with mesoporous structure is maintained. Visibly, extensive aggregation of Ru nanoparticles can be found on the surface of Ru/$SiO_2$ catalyst (Fig. 7(a) and (b)). It is likely that Ru species already existing on the microsphere surface after the calcination are involved in the aggregation and formation of larger agglomerates. Compared with Ru/$SiO_2$, Ru/12%Ti-$SiO_2$ shows substantially less Ru aggregation in Fig. 7(c) and (d). Furthermore, high magnification TEM images along with Fast Fourier Transform (FFT) patterns (Fig. 7(e)) reveal the close contact between (101) plane of anatase $TiO_2$ (d-spacing of 0.35 nm) and (101) plane of metallic Ru (d-spacing of 0.22 nm). This finding is in line with the XRD pattern of Ru/12%Ti-$SiO_2$ (Fig. 8, top-left), in which small diffraction peaks of metallic Ru are observable at 42.0 and 43.8° (JCPDS No. 06-0663), accompanied by the presence of anatase $TiO_2$ (JCPDS No. 21-1272). The crystallinity of the latter does not markedly evolve after the reaction. $TiO_2$ crystallite sizes in Ru/12%Ti-$SiO_2$ before and after the reaction are 7.2 and 7.6 nm, respectively. For Ru/16%Ti-$SiO_2$, $TiO_2$ crystallite sizes before and after the reaction are 7.2 and 7.4 nm, respectively. Regarding the size of Ru, it is difficult to evaluate by XRD due

to peak broadening and overlapping. Additionally, it cannot be estimated from TEM images owing to severe Ru aggregation in case of $Ru/SiO_2$ catalyst and unclear contrast between Ru and Ti species in case of $Ru/12\%Ti\text{-}SiO_2$ catalyst. The XPS spectra of Ru 3d and C 1s regions and Ti 2p region for spent catalysts are also presented in Fig. 8 and Fig. S10. As expected, the proportion of surface metallic Ru increases after the reduction and methanation comparing with the freshly calcined samples (Fig. 5). The surface Ru/(Si+Ti) ratio on all spent catalysts remains similar to the values obtained before the reaction (Table 3). Likewise, the Ti concentrations on the surface of spent catalysts closely match those of freshly calcined catalysts.

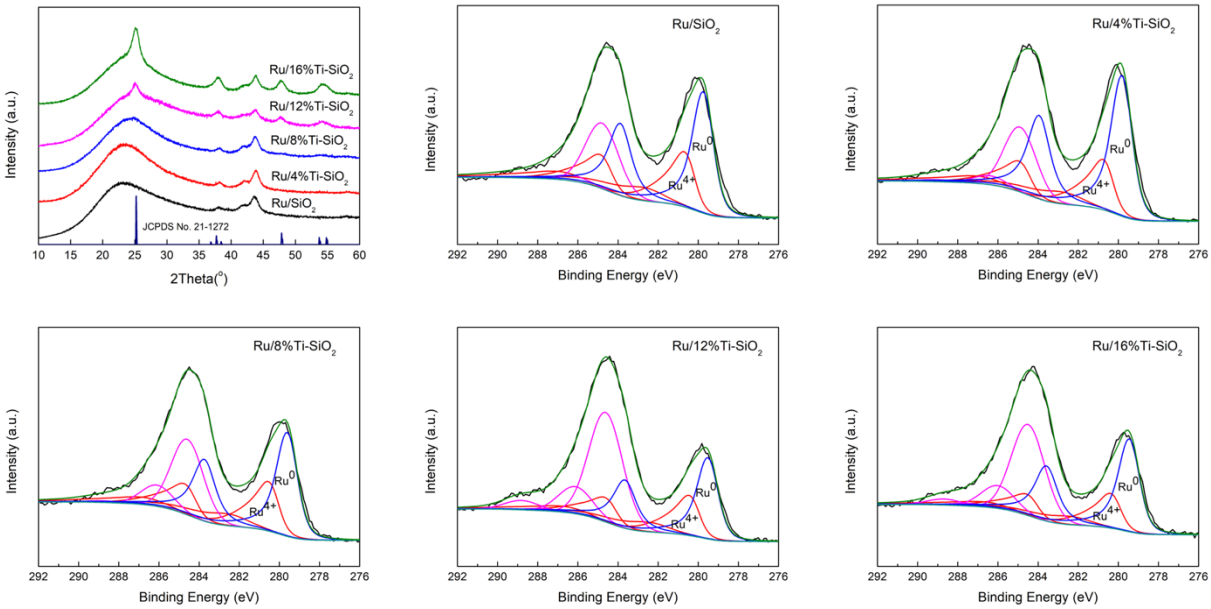


**Fig. 8** XRD patterns (top-left) and XPS spectra of C 1s and Ru 3d regions of spent $Ru/SiO_2$ and $Ru/Ti\text{-}SiO_2$ catalysts.

### 3.4. Decisive factors governing $CO_2$ methanation activity

After impregnation of $RuO_2$ colloidal suspension onto the silica support, the sample was vacuum-dried using the rotavapor and subsequently calcined at 450 °C to remove residual chlorine. This dehydration and thermal treatment can induce the growth of $RuO_2$ crystallites. Fig. 9(a) demonstrates how the evolution of Ti species during catalyst preparation influences the dispersion of $RuO_2$ and final Ru nanoparticles. In $Ti\text{-}SiO_2$ materials, Ti is mainly present as isolated and polymerized species, with the latter becoming more dominant at higher Ti loadings, without forming crystalline $TiO_2$. Upon $RuO_2$ impregnation and calcination, the degree of Ti polymerization increases (as indicated by a decrease in $E_g$), and in high Ti-loading samples ($\geq 12\%$), more concentrated polymerized Ti species are crystallized into small anatase $TiO_2$. The presence of isolated and polymerized Ti species helps suppress aggregation of $RuO_2$

and Ru nanoparticles on $SiO_2$ to some extent, while small anatase $TiO_2$ provides interaction and stabilization of $RuO_2$ and final Ru nanoparticles, forming Ru-$TiO_2$ interface (as shown in Fig. 7(d) and (e)). Additional discussion can be found below Fig. S11 in the Supporting Information.

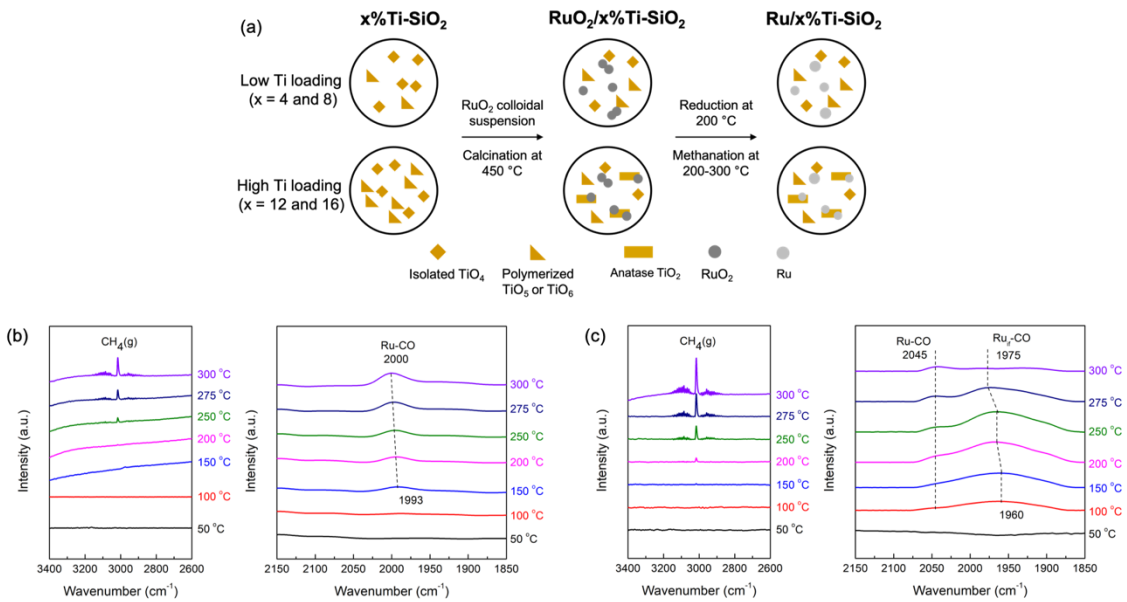


**Fig. 9** (a) Schematic illustration of the evolution of Ti and Ru species in Ru/Ti-$SiO_2$ catalysts with different Ti loadings during wetness impregnation, calcination, $H_2$ reduction and $CO_2$ methanation reaction. DRIFT spectra recorded at steady-state during $CO_2$ methanation from 50 °C to 300 °C on (b) Ru/$SiO_2$ and (c) Ru/12%Ti-$SiO_2$ catalysts.

In-situ DRIFTS experiments under $CO_2/H_2$ mixture were performed to probe the surface intermediate species on the reduced catalysts and possibly obtain information about the active sites, comparing Ru/$SiO_2$ and Ru/12%Ti-$SiO_2$. A detailed discussion together with $CO_2$-TPD analysis (Fig. S13) can be found below Fig. S12 in the Supporting Information. Focusing on the region of carbonyl bands at 2045-1960 $cm^{-1}$ in Fig. 9(b) and (c), we perceive that carbonyl species are formed at the temperature as low as 100 °C for Ru/12%Ti-$SiO_2$. The bands at 2000-1993 $cm^{-1}$ and 2045 $cm^{-1}$ in the spectra of Ru/$SiO_2$ and Ru/12%Ti-$SiO_2$, respectively, can be ascribed to CO linearly adsorbed on Ru sites (Ru-CO). It has been proposed that the wavenumber of this linearly-bonded CO is coverage-dependent. A shift to higher wavenumber is indicative of a larger CO coverage [47]. There is also a marked difference in band intensities at 1975-1960 $cm^{-1}$ between the two catalysts. These bands can be assigned to bridged-bonded CO at the metal-support interface ($Ru_{if}$-CO) [19, 48, 49]. This indicates that for Ru/12%Ti-$SiO_2$, CO adsorption could be facilitated at interfacial sites between Ru and $TiO_2$. Several

studies discuss that interfacial adsorbed carbonyl species are more active intermediates than linear carbonyl and multi-carbonyl species in $CO/CO_2$ methanation reactions either via direct or H-assisted dissociation of adsorbed CO [12, 19, 45]. It is noted that no signal of unreactive multi-carbonyl species at 2130 and 2075 $cm^{-1}$ is detectable in the spectra of either catalyst, as these species are more prevalent on low-coordinated Ru sites of subnanometer-sized metal atoms/clusters [45, 50], which is not the case in the present study. With stepwise increasing temperatures above 200 °C, the $Ru_{if}$-CO band in the Ru/12%Ti-$SiO_2$ spectra starts diminishing. Simultaneously, the band corresponding to gaseous $CH_4$ at 3017 $cm^{-1}$ appears. Additionally, this $CH_4$ band is more intense for Ru/12%Ti-$SiO_2$ than for the undoped catalyst. Taken together, these results suggest that higher concentration of interfacial adsorbed CO could be primarily responsible for higher catalytic activity of the Ti-doped catalyst.

Turning to the possible $CO_2$ methanation mechanism, direct dissociation and H-assisted dissociation of $CO_2$ are two pathways commonly proposed for Ru-based catalysts. The former entails the dissociative $CO_2$ adsorption into adsorbed CO and O, followed by CO hydrogenation to produce $CH_4$ [12, 51, 52]. The alternative involves the reaction of adsorbed $CO_2$ and H to form formate species, which can be further hydrogenated into adsorbed CO and eventually into $CH_4$ [45, 53, 54]. The absence of formate species for Ru/$SiO_2$ is consistent with a direct $CO_2$ dissociation. The current findings also support the direct $CO_2$ dissociation pathway for Ru/12%Ti-$SiO_2$. Although formate species formed at the metal-support interface are known to potentially serve as the source of carbonyl species through their reaction with adsorbed hydrogen [45, 55], the change in formate bands does not correlate with the evolution of CO and $CH_4$ bands, indicating that formates might act only as spectator species. Moreover, it is clear that Ti promoter, existing in the form of anatase, modifies the CO adsorption with the provision of interfacial sites between Ru and $TiO_2$. In the $CO_2$ dissociative pathway, the further dissociation of adsorbed CO or hydrogenation of adsorbed CO is generally recognized as the rate-determining step over Ru-based catalysts [56, 57]. Importantly, this step is more favorable at the interfacial sites with lower energy barrier [19, 54, 58]. The remarkable enhancement of CO adsorption at the interfacial sites over Ru/12%Ti-$SiO_2$ catalyst thus could be the reason for the marked catalytic activity improvement.

## 4. Conclusions

Hierarchically mesoporous Ti-promoted silica materials with high specific surface area and large pores were successfully synthesized via the aerosol-assisted sol-gel process. These materials are able to accommodate homogeneous dispersion of Ti species, up to 16 mol%.

Notably, Ti atoms are highly dispersed in the $SiO_2$ matrix even if a minor fraction of oligomeric or small nanodomains of Ti species are also formed at high loadings. $TiO_2$ nanocrystals are not yet formed at this stage even after calcination at 550°C. This work has shown that Ti species play a marked beneficial role in stabilizing $RuO_2$ nanoparticles, impeding their crystal growth during the calcination. Especially in Ru/12%Ti-$SiO_2$ and Ru/16%Ti-$SiO_2$ catalysts, the impregnation of $RuO_2$ nanoparticles and subsequent calcination induce the crystallization of small anatase $TiO_2$ domains, in turn forming interfacial contact between $RuO_2$ and $TiO_2$. This turned out to strongly affect the methanation activity obtained after in-situ pre-reduction. As a general trend, $CH_4$ formation rate increases with an increase in Ru dispersion. At 300 °C, $CH_4$ formation rate of Ru/12%Ti-$SiO_2$ is 2.3 times higher than that of Ru/$SiO_2$. Our finding that the apparent activation energy is modified upon Ti promotion further suggests that the nature of the active sites is modified by Ti loading. As evidenced by in-situ DRIFTS experiments, $CO_2$ dissociation over Ru/12%Ti-$SiO_2$ catalyst occurs at a temperature as low as 100 °C. Importantly, Ti promoter existing in the form of anatase $TiO_2$ crystallites promotes the adsorption of CO at the metal-support interface, which could be held responsible for the catalytic activity improvement. The present study has helped clarify the promotional effect of Ti on Ru/$SiO_2$ catalysts for $CO_2$ methanation. More broadly, the versatile and highly potent synthesis method presented herein offers the possibility to explore other metal promoters in $CO_2$ methanation.

**Acknowledgement**

The work has been supported by the Southeast Asia-Europe Joint Funding Scheme for Research and Innovation (Project PINT-MULTI/BEJ – R.8001.21). This research has also received funding support from the NSRF via the Program Management Unit for Human Resources & Institutional Development, Research and Innovation [Grant number B16F640034]. The financial support of Grant Agency of Masaryk University (GAMU) is gratefully acknowledged under the grant number MUNI/J/0007/2021. We acknowledge CF CryoEM of CIISB, Instruct-CZ Centre, supported by MEYS CR (LM2023042)) and European Regional Development Fund-Project „UP CIISB“ (No. CZ.02.1.01/0.0/0.0/18_046/0015974). The authors thank Dr. Zuzana Hlavenkova for acquiring STEM-EDS micrographs. Plaifa Hongmanorom thanks the Fonds De La Recherche Scientifique – FNRS (10.13039/501100002661) for her postdoctoral researcher – CR fellowship.

**Data availability**

Data will be made available on request.

## References


[1] G.A. Olah, G.K.S. Prakash, A. Goeppert, Anthropogenic Chemical Carbon Cycle for a Sustainable Future, Journal of the American Chemical Society, 133 (2011) 12881-12898.
[2] A. Rafiee, K. Rajab Khalilpour, D. Milani, M. Panahi, Trends in CO2 conversion and utilization: A review from process systems perspective, Journal of Environmental Chemical Engineering, 6 (2018) 5771-5794.
[3] R.-P. Ye, J. Ding, W. Gong, M.D. Argyle, Q. Zhong, Y. Wang, C.K. Russell, Z. Xu, A.G. Russell, Q. Li, M. Fan, Y.-G. Yao, CO2 hydrogenation to high-value products via heterogeneous catalysis, Nature Communications, 10 (2019) 5698.
[4] S. Roy, A. Cherevotan, S.C. Peter, Thermochemical CO2 Hydrogenation to Single Carbon Products: Scientific and Technological Challenges, ACS Energy Letters, 3 (2018) 1938-1966.
[5] J. Ashok, S. Pati, P. Hongmanorom, Z. Tianxi, C. Junmei, S. Kawi, A review of recent catalyst advances in CO2 methanation processes, Catal. Today, 356 (2020) 471-489.
[6] W. Li, H. Wang, X. Jiang, J. Zhu, Z. Liu, X. Guo, C. Song, A short review of recent advances in CO2 hydrogenation to hydrocarbons over heterogeneous catalysts, RSC Adv., 8 (2018) 7651-7669.
[7] M. Götz, J. Lefebvre, F. Mörs, A. McDaniel Koch, F. Graf, S. Bajohr, R. Reimert, T. Kolb, Renewable Power-to-Gas: A technological and economic review, Renewable Energy, 85 (2016) 1371-1390.
[8] P. Frontera, A. Macario, M. Ferraro, P. Antonucci, Supported Catalysts for CO2 Methanation: A Review, Catalysts, 7 (2017) 59.
[9] M.A.A. Aziz, A.A. Jalil, S. Triwahyono, A. Ahmad, CO2 methanation over heterogeneous catalysts: recent progress and future prospects, Green Chem., 17 (2015) 2647-2663.
[10] C. Molinet-Chinaglia, S. Shafiq, P. Serp, Low Temperature Sabatier CO2 Methanation, ChemCatChem, 16 (2024) e202401213.
[11] J.H. Kwak, L. Kovarik, J. Szanyi, CO2 Reduction on Supported Ru/Al2O3 Catalysts: Cluster Size Dependence of Product Selectivity, ACS Catal., 3 (2013) 2449-2455.
[12] Y. Guo, S. Mei, K. Yuan, D.-J. Wang, H.-C. Liu, C.-H. Yan, Y.-W. Zhang, Low-Temperature CO2 Methanation over CeO2-Supported Ru Single Atoms, Nanoclusters, and Nanoparticles Competitively Tuned by Strong Metal–Support Interactions and H-Spillover Effect, ACS Catal., 8 (2018) 6203-6215.
[13] P. Panagiotopoulou, D.I. Kondarides, X.E. Verykios, Selective methanation of CO over supported Ru catalysts, Appl. Catal., B, 88 (2009) 470-478.
[14] Z. Kowalczyk, K. Stołecki, W. Raróg-Pilecka, E. Miśkiewicz, E. Wilczkowska, Z. Karpiński, Supported ruthenium catalysts for selective methanation of carbon oxides at very low COx/H2 ratios, Appl. Catal., A, 342 (2008) 35-39.
[15] A. Kim, D.P. Debecker, F. Devred, V. Dubois, C. Sanchez, C. Sassoye, CO2 methanation on Ru/TiO2 catalysts: On the effect of mixing anatase and rutile TiO2 supports, Appl. Catal. B, 220 (2018) 615-625.
[16] A.M. Abdel-Mageed, D. Widmann, S.E. Olesen, I. Chorkendorff, J. Biskupek, R.J. Behm, Selective CO Methanation on Ru/TiO2 Catalysts: Role and Influence of Metal–Support Interactions, ACS Catal., 5 (2015) 6753-6763.

[17] A.M. Abdel-Mageed, K. Wiese, M. Parlinska-Wojtan, J. Rabeah, A. Brückner, R.J. Behm, Encapsulation of Ru nanoparticles: Modifying the reactivity toward CO and CO2 methanation on highly active Ru/TiO2 catalysts, Appl. Catal., B, 270 (2020) 118846.
[18] S. Chen, A.M. Abdel-Mageed, M. Li, S. Cisneros, J. Bansmann, J. Rabeah, A. Brückner, A. Groß, R.J. Behm, Electronic metal-support interactions and their promotional effect on CO2 methanation on Ru/ZrO2 catalysts, J. Catal., 400 (2021) 407-420.
[19] M. Gao, J. Zhang, P. Zhu, X. Liu, Z. Zheng, Unveiling the origin of alkali metal promotion in CO2 methanation over Ru/ZrO2, Appl. Catal., B, 314 (2022) 121476.
[20] S. Cisneros, S. Chen, C. Fauth, A.M. Abdel-Mageed, S. Pollastri, J. Bansmann, L. Olivi, G. Aquilanti, H. Atia, J. Rabeah, M. Parlinska-Wojtan, A. Brückner, R.J. Behm, Controlling the selectivity of high-surface-area Ru/TiO2 catalysts in CO2 reduction - modifying the reaction properties by Si doping of the support, Appl. Catal., B, 317 (2022) 121748.
[21] S. Chen, A.M. Abdel-Mageed, C. Gauckler, S.E. Olesen, I. Chorkendorff, R.J. Behm, Selective CO methanation on isostructural Ru nanocatalysts: The role of support effects, J. Catal., 373 (2019) 103-115.
[22] S. Kattel, P. Liu, J.G. Chen, Tuning Selectivity of CO2 Hydrogenation Reactions at the Metal/Oxide Interface, Journal of the American Chemical Society, 139 (2017) 9739-9754.
[23] X. Guo, Z. Peng, A. Traitangwong, G. Wang, H. Xu, V. Meeyoo, C. Li, S. Zhang, Ru nanoparticles stabilized by ionic liquids supported onto silica: highly active catalysts for low-temperature CO2 methanation, Green Chem., 20 (2018) 4932-4945.
[24] K. Furman, D. Baudouin, T. Margossian, K.D. Sabnis, Y. Cui, F.H. Ribeiro, C. Copéret, Increased methanation activity through passivation of the silica support, J. Catal., 324 (2015) 9-13.
[25] J. Polanski, T. Siudyga, P. Bartczak, M. Kapkowski, W. Ambrozkiewicz, A. Nobis, R. Sitko, J. Klimontko, J. Szade, J. Lelątko, Oxide passivated Ni-supported Ru nanoparticles in silica: A new catalyst for low-temperature carbon dioxide methanation, Appl. Catal., B, 206 (2017) 16-23.
[26] D.P. Debecker, S. Le Bras, C. Boissière, A. Chaumonnot, C. Sanchez, Aerosol processing: a wind of innovation in the field of advanced heterogeneous catalysts, Chem. Soc. Rev., 47 (2018) 4112-4155.
[27] C. Boissiere, D. Grosso, A. Chaumonnot, L. Nicole, C. Sanchez, Aerosol Route to Functional Nanostructured Inorganic and Hybrid Porous Materials, Adv. Mater., 23 (2011) 599-623.
[28] H. Wang, Y. Zhang, Y. Zhang, Y. Li, X. Wang, H. Wang, W.D. Wu, X. Bao, Z. Wu, Aerosol Spray Drying Guided Synthesis of Ultrasmall Alloyed Bimetallic Nanoparticles Supported on Silica for Catalytic Semihydrogenation, Small, 19 (2023) 2204744.
[29] V. Smeets, C. Boissière, C. Sanchez, E.M. Gaigneaux, E. Peeters, B.F. Sels, M. Dusselier, D.P. Debecker, Aerosol Route to TiO2–SiO2 Catalysts with Tailored Pore Architecture and High Epoxidation Activity, Chem. Mater., 31 (2019) 1610-1619.
[30] C. Sassoye, G. Muller, D.P. Debecker, A. Karelovic, S. Cassaignon, C. Pizarro, P. Ruiz, C. Sanchez, A sustainable aqueous route to highly stable suspensions of monodispersed nano ruthenia, Green Chem., 13 (2011) 3230-3237.
[31] L. Rochlitz, J.W.A. Fischer, Q. Pessemesse, A.H. Clark, A. Ashuiev, D. Klose, P.-A. Payard, G. Jeschke, C. Copéret, Ti-Doping in Silica-Supported PtZn Propane Dehydrogenation Catalysts: From Improved Stability to the Nature of the Pt–Ti Interaction, JACS Au, 3 (2023) 1939-1951.
[32] F. Bini, C. Rosier, R.P. Saint-Arroman, E. Neumann, C. Dablemont, A. de Mallmann, F. Lefebvre, G.P. Niccolai, J.-M. Basset, M. Crocker, J.-K. Buijink, Surface Organometallic

Chemistry of Titanium: Synthesis, Characterization, and Reactivity of (⋮Si−O)nTi(CH2C(CH3)3)4-n (n = 1, 2) Grafted on Aerosil Silica and MCM-41, Organometallics, 25 (2006) 3743-3760.
[33] R. De Clercq, M. Dusselier, C. Poleunis, D.P. Debecker, L. Giebeler, S. Oswald, E. Makshina, B.F. Sels, Titania-Silica Catalysts for Lactide Production from Renewable Alkyl Lactates: Structure–Activity Relations, ACS Catal., 8 (2018) 8130-8139.
[34] R. Bai, M.T. Navarro, Y. Song, T. Zhang, Y. Zou, Z. Feng, P. Zhang, A. Corma, J. Yu, Titanosilicate zeolite precursors for highly efficient oxidation reactions, Chemical Science, 11 (2020) 12341-12349.
[35] R. De Clercq, M. Dusselier, E. Makshina, B.F. Sels, Catalytic Gas-Phase Production of Lactide from Renewable Alkyl Lactates, Angew. Chem. Int. Ed., 57 (2018) 3074-3078.
[36] J. Ren, Z. Li, S. Liu, Y. Xing, K. Xie, Silica–Titania mixed Oxides: Si–O–Ti Connectivity, Coordination of Titanium, and Surface Acidic Properties, Catal. Lett., 124 (2008) 185-194.
[37] P. Hongmanorom, J. Ashok, G. Zhang, Z. Bian, M.H. Wai, Y. Zeng, S. Xi, A. Borgna, S. Kawi, Enhanced performance and selectivity of CO2 methanation over phyllosilicate structure derived Ni-Mg/SBA-15 catalysts, Appl. Catal., B, 282 (2021) 119564.
[38] X. Gao, S.R. Bare, J.L.G. Fierro, M.A. Banares, I.E. Wachs, Preparation and in-Situ Spectroscopic Characterization of Molecularly Dispersed Titanium Oxide on Silica, J. Phys. Chem. B, 102 (1998) 5653-5666.
[39] J. Kehres, J.G. Jakobsen, J.W. Andreasen, J.B. Wagner, H. Liu, A. Molenbroek, J. Sehested, I. Chorkendorff, T. Vegge, Dynamical Properties of a Ru/MgAl2O4 Catalyst during Reduction and Dry Methane Reforming, J. Phys. Chem. C, 116 (2012) 21407-21415.
[40] T.N. Phaahlamohlaka, D.O. Kumi, M.W. Dlamini, R. Forbes, L.L. Jewell, D.G. Billing, N.J. Coville, Effects of Co and Ru Intimacy in Fischer–Tropsch Catalysts Using Hollow Carbon Sphere Supports: Assessment of the Hydrogen Spillover Processes, ACS Catal., 7 (2017) 1568-1578.
[41] Y. Zhang, L. Li, F. Liu, H. Qi, L. Zhang, W. Guan, Y. Liu, A. Wang, T. Zhang, Synergy between Ru and WOx Enables Efficient Hydrodeoxygenation of Primary Amides to Amines, ACS Catal., 12 (2022) 6302-6312.
[42] C. Fernández, N. Bion, E.M. Gaigneaux, D. Duprez, P. Ruiz, Kinetics of hydrogen adsorption and mobility on Ru nanoparticles supported on alumina: Effects on the catalytic mechanism of ammonia synthesis, J. Catal., 344 (2016) 16-28.
[43] Y. Zhou, J. Wang, L. Liang, Q. Sai, J. Ni, C.-t. Au, X. Lin, X. Wang, Y. Zheng, L. Zheng, L. Jiang, Unraveling the size-dependent effect of Ru-based catalysts on Ammonia synthesis at mild conditions, J. Catal., 404 (2021) 501-511.
[44] S. Carenco, C. Sassoye, M. Faustini, P. Eloy, D.P. Debecker, H. Bluhm, M. Salmeron, The Active State of Supported Ruthenium Oxide Nanoparticles during Carbon Dioxide Methanation, J. Phys. Chem. C, 120 (2016) 15354-15361.
[45] X. Wang, Y. Hong, H. Shi, J. Szanyi, Kinetic modeling and transient DRIFTS–MS studies of CO2 methanation over Ru/Al2O3 catalysts, J. Catal., 343 (2016) 185-195.
[46] G.C. Bond, M.A. Keane, H. Kral, J.A. Lercher, Compensation Phenomena in Heterogeneous Catalysis: General Principles and a Possible Explanation, Catalysis Reviews, 42 (2000) 323-383.
[47] J. Xu, X. Su, H. Duan, B. Hou, Q. Lin, X. Liu, X. Pan, G. Pei, H. Geng, Y. Huang, T. Zhang, Influence of pretreatment temperature on catalytic performance of rutile TiO2-supported ruthenium catalyst in CO2 methanation, J. Catal., 333 (2016) 227-237.

[48] J. Zhou, Z. Gao, G. Xiang, T. Zhai, Z. Liu, W. Zhao, X. Liang, L. Wang, Interfacial compatibility critically controls Ru/TiO2 metal-support interaction modes in CO2 hydrogenation, Nature Communications, 13 (2022) 327.
[49] S.Y. Chin, C.T. Williams, M.D. Amiridis, FTIR Studies of CO Adsorption on Al2O3- and SiO2-Supported Ru Catalysts, J. Phys. Chem. B, 110 (2006) 871-882.
[50] P. Panagiotopoulou, X.E. Verykios, Mechanistic Study of the Selective Methanation of CO over Ru/TiO2 Catalysts: Effect of Metal Crystallite Size on the Nature of Active Surface Species and Reaction Pathways, J. Phys. Chem. C, 121 (2017) 5058-5068.
[51] S. Navarro-Jaén, J.C. Navarro, L.F. Bobadilla, M.A. Centeno, O.H. Laguna, J.A. Odriozola, Size-tailored Ru nanoparticles deposited over γ-Al2O3 for the CO2 methanation reaction, Appl. Surf. Sci., 483 (2019) 750-761.
[52] S. Eckle, H.-G. Anfang, R.J. Behm, Reaction Intermediates and Side Products in the Methanation of CO and CO2 over Supported Ru Catalysts in H2-Rich Reformate Gases, J. Phys. Chem. C, 115 (2011) 1361-1367.
[53] M.R. Prairie, A. Renken, J.G. Highfield, K. Ravindranathan Thampi, M. Grätzel, A fourier transform infrared spectroscopic study of C02 methanation on supported ruthenium, J. Catal., 129 (1991) 130-144.
[54] P. Panagiotopoulou, D.I. Kondarides, X.E. Verykios, Mechanistic aspects of the selective methanation of CO over Ru/TiO2 catalyst, Catal. Today, 181 (2012) 138-147.
[55] S. Cisneros, L. Santa-Taborda, L. Martínez Quintana, A.I.M. Rabee, H. Abed, N. Rockstroh, S. Bartling, M. Romero-Sáez, H. Atia, A. Belén Dongil, A. Brückner, J. Rabeah, The effect of O-vacancies on intermediates stability and electron delocalization over MgO modified Ru/ZrO2: Spectroscopic insights during CO2 methanation, Chem. Eng. J., 474 (2023) 145646.
[56] B. Miao, S.S.K. Ma, X. Wang, H. Su, S.H. Chan, Catalysis mechanisms of CO2 and CO methanation, Catal. Sci. Technol., 6 (2016) 4048-4058.
[57] X. Li, J. Lin, L. Li, Y. Huang, X. Pan, S.E. Collins, Y. Ren, Y. Su, L. Kang, X. Liu, Y. Zhou, H. Wang, A. Wang, B. Qiao, X. Wang, T. Zhang, Controlling CO2 Hydrogenation Selectivity by Metal-Supported Electron Transfer, Angew. Chem. Int. Ed., 59 (2020) 19983-19989.
[58] P. Panagiotopoulou, D.I. Kondarides, X.E. Verykios, Mechanistic Study of the Selective Methanation of CO over Ru/TiO2 Catalyst: Identification of Active Surface Species and Reaction Pathways, J. Phys. Chem. C, 115 (2011) 1220-1230.